Contrib Mineral Petrol (2016) 171:106
DOI 10.1007/s00410-016-1314-0

ORIGINAL PAPER

Geochronological and isotopic records of crustal storage and assimilation in the Wolverine Creek–Conant Creek system, Heise eruptive centre, Snake River Plain

D. Szymanowski[1] · B. S. Ellis[1] · J. F. Wotzlaw[1,2] · Y. Buret[1] · A. von Quadt[1] · I. Peytcheva[1] · I. N. Bindeman[3] · O. Bachmann[1]

Received: 11 August 2016 / Accepted: 31 October 2016 / Published online: 19 November 2016

Abstract Understanding the processes of differentiation of the Yellowstone–Snake River Plain (YSRP) rhyolites is typically impeded by the apparent lack of erupted intermediate compositions as well as the complex nature of their shallow interaction with the surrounding crust responsible for their typically low O isotopic ratios. A pair of normal-$\delta^{18}O$ rhyolitic eruptions from the Heise eruptive centre in eastern Idaho, the Wolverine Creek Tuff and the Conant Creek Tuff, represent unique magmatic products of the Yellowstone hotspot preserving abundant vestiges of the intermediate differentiation steps leading to rhyolite generation. We address both shallow and deep processes of magma generation and storage in the two units by combining high-precision ID–TIMS U–Pb zircon geochronology, trace element, O and Hf isotopic studies of zircon, and Sr isotopic analyses of individual high-Mg# pyroxenes inherited from lower- to mid-crustal differentiation stages. The zircon geochronology confirms the derivation of both tuffs from the same rhyolitic magma reservoir erupted at 5.5941 ± 0.0097 Ma, preceded by at least 92 ± 14 ky of continuous or intermittent zircon saturation approximating the length of pre-eruptive magma accumulation in the upper crust. Some low-Mg# pyroxenes enclosing zircons predate the eruption by at least 45 ± 27 ky, illustrating the co-crystallisation of major and accessory phases in the near-liquidus rhyolitic melts of the YSRP over a significant period of time. Coeval zircon crystals are isotopically heterogeneous (two populations at εHf ~−5 and −13), requiring the assembly of isotopically distinct melt pockets directly prior to, or during, the eruption. The primitive Mg# 60–90 pyroxenes are out of isotopic equilibrium with the host rhyolitic melt ($^{87}Sr/^{86}Sr_i = 0.70889$), covering a range of $^{87}Sr/^{86}Sr_i = 0.70705$–$0.70883$ corresponding to ratios typical of the most radiogenic YSRP basalts to the least radiogenic YSRP rhyolites. Together with the low εHf in zircon, the Sr isotopic ratios illustrate limited assimilation dominated by radiogenic Archean crustal source materials incorporated into variably evolved YSRP melts as they progress towards rhyolitic compositions by assimilation–fractional crystallisation.

Keywords Heise · Yellowstone hotspot · Zircon · U–Pb geochronology · Sr isotopes · Pyroxene

Introduction

The geological processes and timescales of generation and accumulation of large, 'super-eruptive' volumes of highly evolved magma remain topics of intense debate, with marked differences in apparent magma accumulation timescales recognised between eruptive products of broadly subduction-related and intraplate tectonic settings, associated with contrasts in e.g. crystallinity, magmatic temperatures, or volatile contents (Bachmann and Bergantz 2008;

Communicated by Othmar Müntener.

Electronic supplementary material The online version of this article (doi:10.1007/s00410-016-1314-0) contains supplementary material, which is available to authorized users.

✉ D. Szymanowski
dawid.szymanowski@erdw.ethz.ch

[1] Institute of Geochemistry and Petrology, Department of Earth Sciences, ETH Zürich, 8092 Zürich, Switzerland

[2] Section of Earth and Environmental Sciences, University of Geneva, 1205 Geneva, Switzerland

[3] Department of Geological Sciences, University of Oregon, Eugene, OR 97403, USA

Christiansen and McCurry 2008; Wolff et al. 2015). It is increasingly observed in arc settings that the geochronological record of zircon crystals found in evolved melts preserves evidence for an extended period of crystallisation of up to a few hundred thousand years (e.g. Reid et al. 1997; Brown and Fletcher 1999; Claiborne et al. 2010; Wotzlaw et al. 2013; Guillong et al. 2014). Such longevity is likely related to long-term thermal buffering of these systems near or below the zircon saturation temperature by repeated inputs of recharge magma, balanced by conduction-dominated cooling (Mahood 1990; Bachmann and Bergantz 2004; Gelman et al. 2013; Cooper and Kent 2014). In contrast, within intraplate volcanic centres, such as the iconic Yellowstone–Snake River Plain (YSRP) volcanic province in the north-western USA, the apparent spread of individual zircon ages appears to be limited to a few tens of thousands of years (Rivera et al. 2014; Wotzlaw et al. 2014, 2015). It remains unclear whether such a zircon record always indicates a true rapid crystallisation/assembly timescale in the Yellowstone hotspot system, or whether such data represent the last cooling events whereas most older zircon crystals are efficiently resorbed during preceding reheating events. While cool, wet, crystal-rich super-eruptions are thought to mobilise near-solidus crystal mushes providing an effective long-term insulation of the magmatic reservoir (Marsh 1981; Bachmann and Bergantz 2004; Hildreth 2004), the evidence of such a mechanism increasing the survivability of the hot, crystal-poor magmas of the YSRP is less obvious (Ellis et al. 2014).

In addition to the discussion of the longevity of YSRP rhyolites, the details of the magmatic evolution responsible for generating large volumes of YSRP rhyolite with subordinate basalt yet no erupted intermediate composition magmas remain contentious. The trace element and radiogenic isotope records indicate that the rhyolites likely originate from mantle-derived basaltic parents with important assimilation of Archean basement rocks (e.g. 7–40%, preferred 12%, McCurry and Rodgers 2009; 45–65%, Hildreth et al. 1991 or >60%, Nash et al. 2006). Moreover, the light oxygen isotope compositions of many YSRP rhyolites have been used to argue for an important contribution from melting of shallow, young, and hydrothermally altered crust (Bindeman and Valley 2001; Boroughs et al. 2005; Bindeman et al. 2007; Watts et al. 2011; Boroughs et al. 2012; Simakin and Bindeman 2012). Such massive amounts of assimilation of cold crustal rocks seem at odds with thermal constraints during assimilation–fractional crystallisation (e.g. Thompson et al. 2002; Bohrson et al. 2014). While it appears that a large part of the radiogenic isotope record may be sourced already from the interaction of the Yellowstone plume with deep crust or lithospheric mantle (Doe et al. 1982; Hanan et al. 2008; McCurry and Rodgers 2009; Jean et al. 2014), the exact crustal evolutionary path of YSRP melts from primitive basalts to the

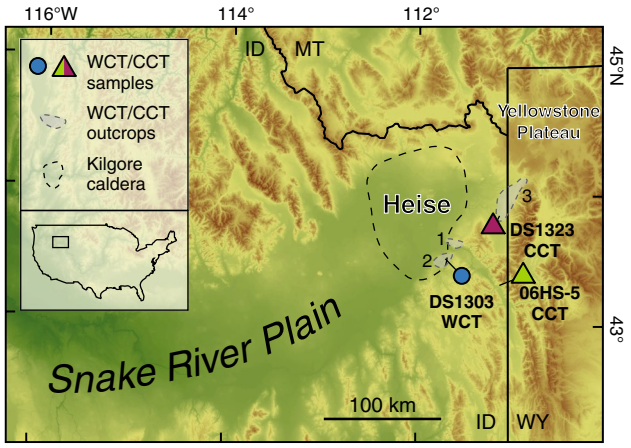

Fig. 1 Location of the Heise eruptive centre in the eastern Snake River Plain. The *black dashed line* illustrates the approximate position of the Heise caldera (Kilgore Tuff caldera of Morgan and McIntosh 2005). The *grey shading* schematically represents outcrop areas of both studied units in the Big Hole Mountains (1), northern Caribou Range (2), and the north-western part of the Teton Range (3). *Symbols* indicate localities of Wolverine Creek Tuff (WCT) and Conant Creek Tuff (CCT) samples used in this study (for coordinates, see Supplementary material)

erupted rhyolites remains enigmatic. Geophysical evidence suggests the existence of low-melt content, intermediate magmatic storage levels throughout the crust underneath the YSRP (Sparlin et al. 1982; Peng and Humphreys 1998; DeNosaquo et al. 2009; Farrell et al. 2014; Huang et al. 2015), but direct sampling of these lithologies parental to the rhyolites has been scarce to absent.

In this contribution, we focus on two normal-$\delta^{18}O$ to slightly ^{18}O-depleted ($\delta^{18}O_{melt} = 5.9$ and 6.5‰; Watts et al. 2011) rhyolitic ignimbrites from the Heise volcanic field in Idaho, the Wolverine Creek Tuff and Conant Creek Tuff, previously shown to preserve vestiges of intermediate composition magmas inferred to complete the basalt–rhyolite fractionation sequence (Szymanowski et al. 2015). The choice of normal-$\delta^{18}O$ units with O isotopic ratios characteristic for purely mantle-derived melts is of particular importance as it limits the probability of shallow-crustal melting of hydrothermally altered crust in generating these rhyolites, and provides a rare glimpse into the deeper processes of rhyolite genesis. We combine high-precision ID–TIMS zircon U–Pb geochronology with radiogenic isotope studies of zircon (Hf) and pyroxene (Sr) crystals to address both shallow and deep processes of magma generation and pre-eruptive storage.

Geological background

The Heise volcanic field in the eastern Snake River Plain, Idaho (Fig. 1), active between 6.6 and 4 Ma (Morgan and

McIntosh 2005; Bindeman et al. 2007; Watts et al. 2011), is the second-youngest eruptive centre of the Yellowstone hotspot track, preceding the main period of activity of the Yellowstone Plateau volcanic field by approximately 2 million years (Christiansen 2001). The eruptive record at Heise is dominated by a series of voluminous (100–1000s km^3) explosive eruptions of high-silica rhyolite followed by effusions of basaltic lavas filling the topographical low of the Snake River Plain. The rhyolitic magma produced within the whole YSRP system ('Snake River-type' rhyolites of Branney et al. 2008) is typically hot ($T > 800$ °C, e.g. Cathey and Nash 2004; Watts et al. 2011), dry (≤2.5 wt% H_2O, e.g. Bolte et al. 2015), and crystal-poor with an anhydrous mineral assemblage of plagioclase ± sanidine ± quartz + augite ± pigeonite ± orthopyroxene ± fayalitic olivine ± ilmenite ± magnetite + accessory zircon, apatite, allanite/chevkinite (Christiansen 2001; Ellis et al. 2013). Most notably, the vast majority of YSRP rhyolites, including some Heise units, have a low $\delta^{18}O$ signature ($\delta^{18}O_{magma} < 5.5‰$) requiring an involvement of hydrothermally altered crust (Hildreth et al. 1984; Bindeman and Valley 2001; Bindeman et al. 2007; Watts et al. 2011).

Within the Heise sequence, two of the normal-$\delta^{18}O$ rhyolitic ignimbrites, the Wolverine Creek Tuff (WCT) and the Conant Creek Tuff (CCT), share a number of features hinting at their common provenance. Both units were previously dated at around 5.5 Ma (Morgan and McIntosh 2005; Bindeman et al. 2007; Anders et al. 2014), but despite the multiple existing $^{40}Ar/^{39}Ar$ and U–Pb dates, the relative timing of the eruptive events producing both deposits is not fully resolved. The two ignimbrites are distinct in the outcrops owing to different degrees of welding; the WCT occurs as a non-welded, crystal-poor ignimbrite dominantly composed of microvesicular pumice clasts and bubble wall shards as well as angular to sub-rounded clasts of black glass; the CCT bears resemblance to other 'SR-type' rhyolites being crystal-poor and densely welded with a dominant devitrified zone associated with a basal vitrophyre (Morgan and McIntosh 2005). The two units only occur in stratigraphic contact at one locality where the CCT overlies the WCT with no clear depositional break (Phillips et al. 2016). However, despite the macroscopic differences, the mineral and glass major and trace element chemistry of both units is indistinguishable, suggesting that they derive from a single magma reservoir (see Szymanowski et al. 2015 for a detailed discussion). In addition to the typical rhyolitic mineral cargo, both WCT and CCT contain a proportion of relatively primitive clinopyroxene of Mg# ~ 60–90 (Fig. 2a) and plagioclase of $An_{38–63}$, often found within crystal aggregates, interpreted to represent parts of a cumulate body that was remobilised and partly incorporated into the rhyolitic magma chamber. The primitive pyroxene crystals enclose intermediate (57–67 wt% SiO_2) melt inclusions (Fig. 2b)

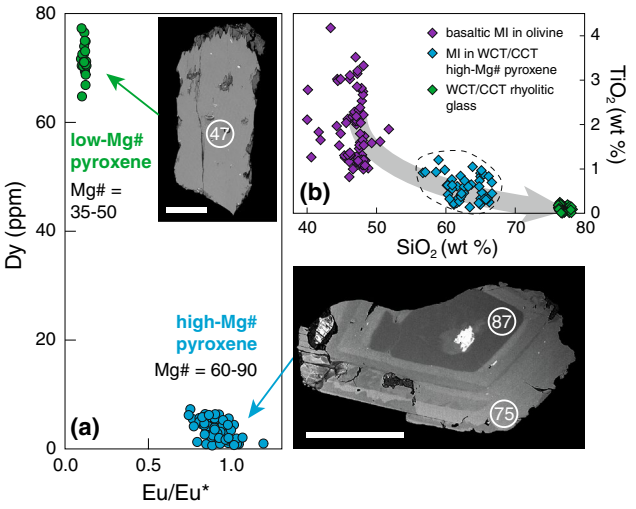

Fig. 2 Summary of the bimodal mineral chemistry within the Wolverine Creek and Conant Creek tuffs (Szymanowski et al. 2015). **a** Two kinds of clinopyroxene found within WCT/CCT differing in Mg#, REE contents (here Dy), Eu/Eu* and internal compositional zonation patterns illustrated with backscatter electron images of representative pyroxene crystals from both groups (*numbers in circles* denote Mg#). The *white bars* in both images are 250 μm long. **b** TiO_2–SiO_2 concentrations in melt inclusions (MI) hosted by the high-Mg# WCT pyroxene crystals compared to the host WCT volcanic glass and melt inclusions in olivine from Snake River Plain basalts (Stefano et al. 2010). The *grey arrow* illustrates a trend in melt composition consistent with (assimilation–) fractional crystallisation of SRP basalts to produce rhyolitic melts of the WCT/CCT

recording magmatic liquids that bridge the compositional gap between basalts and rhyolites and thus support the fractional crystallisation component of magmatic differentiation within the two units. In addition, bulk isotopic data with $^{87}Sr/^{86}Sr$ ratios of 0.7089 for CCT and 0.7095 for WCT (Watts et al. 2011), as well as εNd between −5.2 and −6.8 (Nash et al. 2006; Watts et al. 2011), require a significant amount of assimilated material to account for the shift from the primitive plume-derived basalts ('Imnaha component') at $^{87}Sr/^{86}Sr$ ~0.704 and εNd ~+4 (Wolff et al. 2008).

Methods

Zircon geochemistry

A total of 27 zircon crystals from the Wolverine Creek Tuff ($n = 14$) and Conant Creek Tuff ($n = 13$, including three crystals liberated from clinopyroxene separates used for Sr isotope determination) were analysed for U–Pb isotopes by isotope dilution-thermal ionisation mass spectrometry (ID–TIMS) at the University of Geneva (CCT; Wotzlaw et al. 2015) and ETH Zürich (WCT, px-hosted CCT; von Quadt et al. 2016). Prior to analysis, ~30 crystals per sample were

separated following standard procedures and annealed by heating to 900 °C for 48 h in a muffle furnace. Individual zircons were then selected under a binocular microscope and mounted in epoxy resin, polished, and imaged using cathodoluminescence and backscattered electron microscopy, then analysed for trace elements by LA–ICPMS (WCT, CCT) and by SIMS for O isotopes (CCT). LA–ICPMS analyses included U–Pb isotopes in order to detect inherited cores, but no xenocrysts were found.

Trace element concentrations were determined by LA–ICPMS using a 193 nm ArF excimer laser coupled to a Thermo Element ICP mass spectrometer at the University of Lausanne (CCT) or ETH Zürich (WCT), using NIST 612/610 glass as the primary standard. Both cores and rims were analysed in each crystal with a spot size of 20/25 µm. Repeat analyses of zircon standards yielded external reproducibility (2 RSD) between 2.9% (Hf) and 23.9% (Nd) with the low-abundance Pr reproducible within 57%. Oxygen isotope analyses of CCT zircons were performed at the Canadian Centre for Isotopic Microanalysis, University of Alberta, employing a Cameca IMS1280 secondary ion mass spectrometer (see Wotzlaw et al. 2015 for details). Repeat analyses of primary reference zircons (Mud Tank zircon, $\delta^{18}O_{VSMOW} = +4.87‰$) yielded within-session reproducibility between ±0.14 and 0.20‰ (2σ) that was propagated into the uncertainty of samples yielding an average single-spot uncertainty of ±0.25‰. Analyses of secondary reference zircon Temora-2 ($\delta^{18}O_{VSMOW} = +8.20‰$; Black et al. 2004) yielded a weighted mean $\delta^{18}O_{VSMOW}$ of +8.260 ± 0.061‰ (MSWD = 1.6; $n = 18$).

After LA–ICPMS/SIMS analyses, selected individual crystals were extracted from the grain mount, transferred into 3 ml Savillex beakers, rinsed with 3 N HNO_3, and loaded into 200 µl Savillex microcapsules for partial dissolution in HF + trace HNO_3 at 180 °C for 12 h ('chemical abrasion (CA)'; Mattinson 2005). The abraded crystals were transferred back into 3 ml beakers for cleaning with 6 N HCl and 3 N HNO_3, then reloaded into their respective 200-µl microcapsules, spiked with 3–9 mg of the EARTHTIME ^{202}Pb–^{205}Pb–^{233}U–^{235}U tracer solution (Condon et al. 2015; McLean et al. 2015), and dissolved in HF + trace HNO_3 at 210 °C for ~60 h. After dissolution, samples were dried down and redissolved in 6 N HCl at 180 °C for ~12 h to convert to chlorides, then dried down again and taken up in 3 N HCl. Pb and U were separated from the matrix using an HCl-based single-column anion exchange chemistry modified from Krogh (1973); the remaining eluted fraction ('wash') was collected for Hf isotopic analyses. The U–Pb fractions were dried down with a drop of 0.035 M H_3PO_4 and loaded on single outgassed Re filaments with a silica gel emitter modified from Gerstenberger and Haase (1997). U and Pb measurements were performed with a Thermo TRITON (UNIGE) or TRITON Plus (ETH) thermal ionisation mass spectrometer; Pb was measured in dynamic mode on a MasCom secondary electron multiplier and U was measured as UO_2 in static mode on Faraday cups equipped either with 10^{12} Ω resistors (UNIGE) or 10^{13} Ω resistors (ETH; von Quadt et al. 2016). Pb mass fractionation factors were derived from the measured $^{202}Pb/^{205}Pb$ ratio normalised to the true value of 0.99924 (Condon et al. 2015). U isotopic ratios were corrected for isobaric interferences of $^{233}U^{18}O^{16}O$ on $^{235}U^{16}O_2$ using an $^{18}O/^{16}O$ of 0.00205 ± 0.00005 and for mass fractionation using the measured $^{233}U/^{235}U$ ratio relative to the true value of 0.99506 (Condon et al. 2015) and sample $^{238}U/^{235}U$ of 137.818 ± 0.045 (Hiess et al. 2012). All common Pb in zircon analyses was attributed to laboratory blank and corrected with the average composition of total procedural blank measurements. Data reduction was performed using the Tripoli and U–Pb_Redux software packages (Bowring et al. 2011) using data reduction and uncertainty propagation algorithms of McLean et al. (2011). U–Pb ratios and dates were calculated relative to a tracer $^{235}U/^{205}Pb$ ratio of 100.23 ± 0.046% (2σ) and using the decay constants of Jaffey et al. (1971). $^{206}Pb/^{238}U$ ratios and dates were corrected for initial ^{230}Th disequilibrium using Th/U of 3.39 ± 0.12 (2σ, $n = 124$) measured in WCT/CCT glass by Szymanowski et al. (2015); whole-grain Th/U of zircon crystals (Table 1) is relatively homogeneous at 0.58 ± 0.22 (2σ), similar to rim values of 0.51 ± 0.30 (Fig. 5) considered to be in equilibrium with the glass. All uncertainties are reported at the 2σ level and ignore systematic uncertainties associated with the tracer calibration and decay constants (Jaffey et al. 1971; McLean et al. 2015).

Hf isotopic compositions of single zircons were analysed in eluted fractions remaining from U–Pb anion exchange chemistry. Hf was either separated using an HCl–HF-based column chemistry using the Ln-spec resin and analysed on a Nu Plasma II MC-ICPMS at ETH Zürich (WCT, px-hosted CCT), or analysed on a Thermo Neptune Plus MC-ICPMS at the University of Geneva without chemical separation (CCT; see D'Abzac et al. 2016 for details). All $^{176}Hf/^{177}Hf$ isotope ratios were normalised to the JMC475 standard (recommended value of $^{176}Hf/^{177}Hf = 0.282160$; Vervoort and Blichert-Toft 1999), which returned highly reproducible values over the course of three sessions at 0.282186 ± 10 (2σ, $n = 29$), 0.282153 ± 12 ($n = 11$), and 0.282153 ± 22 ($n = 35$). A minimal correction for in situ ingrowth of ^{176}Hf due to ^{176}Lu decay was calculated using the ^{176}Lu decay constant of Scherer et al. (2001), with $^{176}Lu/^{177}Hf$ directly measured (CCT) or derived from Lu/Hf measured via LA–ICPMS (WCT). All reported uncertainties include the within-run precision of each measurement and the reproducibility of the JMC475 standard.

Table 1 CA–ID–TIMS U–Pb isotopic data for WCT/CCT zircon

Sample	Composition				Isotopic ratios								Dates (Ma)					
	Th/U[a]	Pb* (pg)[b]	Pb_c (pg)[c]	Pb*/Pb_c[d]	$^{206}Pb/^{204}Pb$[e]	$^{206}Pb/^{238}U$[f]	±2σ (%)	$^{207}Pb/^{235}U$[f]	±2σ (%)	$^{207}Pb/^{206}Pb$[f]	±2σ (%)	Corr. coef.	$^{206}Pb/^{238}U$[g]	±2σ (abs)	$^{206}Pb/^{238}U$ < Th >[h]	±2σ (abs)	$^{207}Pb/^{235}U$[g]	±2σ (abs)
Conant Creek Tuff																		
z1	0.52	1.16	0.13	9.04	534	0.0008591	0.18	0.00544	3.99	0.0459	3.86	0.712	5.5357	0.0098	5.6281	0.0095	5.52	0.22
z2	0.59	1.75	0.09	20.46	1164	0.0008592	0.09	0.00565	1.73	0.0477	1.68	0.671	5.5364	0.0048	5.6266	0.0047	5.718	0.099
z3	0.67	1.22	0.14	8.68	494	0.0008603	0.23	0.00535	4.67	0.0451	4.52	0.699	5.544	0.013	5.631	0.012	5.41	0.25
z4	0.50	2.26	0.23	10.01	592	0.0008599	0.17	0.00553	3.54	0.0467	3.42	0.689	5.5408	0.0094	5.6338	0.0092	5.60	0.20
z5	0.58	0.77	0.10	8.03	468	0.0008620	0.22	0.00574	4.41	0.0483	4.25	0.719	5.555	0.012	5.645	0.012	5.81	0.26
z6	0.50	0.71	0.09	8.04	478	0.0008606	0.22	0.00556	4.43	0.0468	4.28	0.708	5.545	0.012	5.638	0.012	5.63	0.25
z7	0.55	1.88	1.45	1.30	90	0.0008594	1.02	0.00690	21.34	0.0583	20.59	0.752	5.538	0.056	5.629	0.054	7.0	1.5
z8	0.63	0.47	0.77	0.61	51	0.0008647	2.24	0.00817	39.62	0.0686	37.97	0.752	5.57	0.12	5.66	0.12	8.3	3.3
z9	0.52	2.99	0.41	7.29	433	0.0008624	0.19	0.00583	4.50	0.0490	4.37	0.726	5.557	0.011	5.649	0.010	5.90	0.26
z10	0.48	0.23	0.13	1.78	121	0.0008539	0.82	0.00514	21.12	0.0436	20.51	0.754	5.502	0.045	5.596	0.044	5.2	1.1
Pyroxene-hosted Conant Creek Tuff																		
Px12-1	0.55	1.31	0.62	2.11	141	0.0008580	0.39	0.00602	6.78	0.0509	6.54	0.638	5.529	0.022	5.620	0.021	6.09	0.41
Px11-1	0.98	2.36	0.71	3.34	194	0.0008623	0.35	0.00575	5.10	0.0484	4.93	0.506	5.557	0.020	5.634	0.019	5.82	0.30
Px12-2	0.59	1.19	0.74	1.61	111	0.0008612	0.47	0.00613	8.52	0.0517	8.24	0.615	5.549	0.026	5.639	0.026	6.21	0.53
Wolverine Creek Tuff																		
z3	0.86	0.67	0.17	3.98	234	0.0008557	0.36	0.00568	5.91	0.0482	5.63	0.774	5.514	0.020	5.596	0.020	5.75	0.34
z6	0.55	0.33	0.28	1.21	89	0.0008624	0.65	0.00630	11.51	0.0530	11.11	0.641	5.557	0.036	5.649	0.035	6.38	0.73
z7	0.52	0.87	0.16	5.40	337	0.0008591	0.18	0.00573	3.06	0.0484	2.94	0.663	5.5360	0.0099	5.6283	0.0097	5.80	0.18
z10	0.49	0.67	0.20	3.35	217	0.0008558	0.30	0.00581	4.95	0.0492	4.75	0.711	5.515	0.016	5.608	0.016	5.88	0.29
z11	0.53	0.35	0.15	2.27	152	0.0008618	0.48	0.00607	8.10	0.0511	7.75	0.740	5.553	0.026	5.645	0.026	6.14	0.50
z13	0.61	0.46	0.18	2.58	167	0.0008577	0.63	0.00564	10.21	0.0477	9.70	0.817	5.527	0.035	5.616	0.034	5.71	0.58
z14	0.68	0.68	0.13	5.28	317	0.0008690	0.18	0.00591	3.81	0.0493	3.69	0.651	5.5992	0.0099	5.6866	0.0096	5.98	0.23
z15	0.58	5.94	0.21	28.56	1678	0.0008648	0.10	0.00568	0.74	0.0477	0.67	0.687	5.5724	0.0055	5.6629	0.0054	5.753	0.042
z16	0.48	0.81	0.16	5.23	330	0.0008536	0.18	0.00575	3.04	0.0489	2.92	0.682	5.501	0.010	5.5941	0.0097	5.83	0.18
z17	0.52	0.17	0.20	0.85	69	0.0008678	1.77	0.00723	33.64	0.0605	32.28	0.779	5.592	0.099	5.684	0.095	7.3	2.5
z18	0.50	0.65	0.18	3.68	237	0.0008617	0.29	0.00590	4.65	0.0497	4.46	0.694	5.552	0.016	5.645	0.016	5.98	0.28
z21	0.52	0.86	0.12	7.48	460	0.0008631	0.14	0.00578	2.40	0.0486	2.31	0.682	5.5617	0.0080	5.6541	0.0078	5.86	0.14

Table 1 continued

Sample	Composition				Isotopic ratios							Dates (Ma)					
	Th/U^{a}	Pb* (pg)[b]	Pb_c (pg)[c]	Pb*/Pb_c[d]	$^{206}Pb/^{204}Pb$[e]	$^{206}Pb/^{238}U$[f]	±2σ (%)	$^{207}Pb/^{235}U$[f]	±2σ (%)	$^{207}Pb/^{206}Pb$[f]	±2σ (%)	Corr. coef.	$^{206}Pb/^{238}U$[g]	±2σ (abs)	$^{206}Pb/^{238}U$ < Th >[h]	±2σ (abs)	$^{207}Pb/^{235}U$[g]	±2σ (abs)
z25	0.67	0.77	0.19	4.07	249	0.0008573	0.30	0.00572	4.72	0.0484	4.52	0.702	5.524	0.016	5.612	0.016	5.80	0.27
z31	0.49	0.24	0.22	1.08	82	0.0009211	1.08	0.00703	16.93	0.0554	16.08	0.800	5.935	0.064	6.028	0.062	7.1	1.2

[a] Th contents calculated from radiogenic ^{208}Pb and the ^{230}Th-corrected $^{206}Pb/^{238}U$ date of the sample, assuming concordance between the U–Pb and Th–Pb systems

[b] Total mass of radiogenic Pb

[c] Total mass of common Pb

[d] Ratio of radiogenic Pb (including ^{208}Pb) to common Pb

[e] Measured ratio corrected for fractionation and spike contribution only

[f] Measured ratios corrected for fractionation, tracer, and blank. Blank was corrected using the average composition of total procedural blank measurements taken throughout the course of the study in both laboratories. At University of Geneva (CCT): $^{206}Pb/^{204}Pb = 17.618 \pm 0.368$, $^{207}Pb/^{204}Pb = 14.730 \pm 0.450$, $^{208}Pb/^{204}Pb = 35.77 \pm 1.07$ ($n = 10$), at ETH Zurich (WCT): $^{206}Pb/^{204}Pb = 18.407 \pm 0.197$, $^{207}Pb/^{204}Pb = 15.191 \pm 0.194$, $^{208}Pb/^{204}Pb = 36.926 \pm 0.453$ ($n = 18$). All uncertainties are 1σ

[g] Isotopic dates calculated using the decay constants $\lambda(^{238}U) = 1.55125 \times 10^{-10}$ and $\lambda(^{235}U) = 9.8485 \times 10^{-10}$ $year^{-1}$ (Jaffey et al. 1971)

[h] Corrected for initial Th/U disequilibrium using radiogenic ^{208}Pb and Th/U_{melt} of 3.39 ± 0.12 (2σ)

$^{87}Sr/^{86}Sr$ in pyroxene and glass

The high-Mg# clinopyroxenes from the Wolverine Creek Tuff are sufficiently large and rich in Sr (50–260 ppm) that single pyroxenes could be analysed for $^{87}Sr/^{86}Sr$ using thermal ionisation mass spectrometry (TIMS); the evolved (low-Mg#, <15 ppm Sr) clinopyroxene separated from other Heise units required bulk mineral separates of 10–20 grains (2–4 mg). For glass, large separates of 7.1 and 9.4 mg were hand-picked from crushed samples. The separates were digested with a concentrated HF/HNO_3 mixture in Teflon beakers for 3 days (glass) or 24 h (pyroxene); after evaporation, they were redissolved in 6 N HCl for 12 h. All solutions were evaporated, and the dry residues were converted in 2.5 N HNO_3, followed by Sr separation in PP ion exchange columns with Sr- and TRU-spec resins, employing the chromatography technique of Pin et al. (1994). Strontium isotope ratios were measured on a Thermo TRITON Plus multicollector TIMS at ETH Zürich in static mode. The Sr isotope ratios are mass fractionation corrected to $^{88}Sr/^{86}Sr = 8.375209$; the NBS 987 standard measurements returned $^{87}Sr/^{86}Sr = 0.7102460 \pm 34$ (2 se; $n = 14$) during the period of analysis. Rb and Sr concentrations of most samples were determined by isotope dilution using a highly enriched $^{87}Rb/^{84}Sr$ spike. All $^{87}Sr/^{86}Sr$ ratios are reported as initial values using Rb/Sr measured by TIMS, LA–ICPMS (Szymanowski et al. 2015) or assumed based on similarity to other samples; all corrected to $^{40}Ar/^{39}Ar$ ages of Morgan and McIntosh (2005).

Results

The zircon record

Three kinds of zircon crystals were analysed in this study: bulk-rock-separated WCT zircons, bulk-rock-separated CCT zircons, and pyroxene-hosted CCT zircons recovered from low-Mg# clinopyroxene samples dissolved for Sr isotopic analyses (Px11, Px12, Px19). All three samples return overlapping zircon age distributions (Fig. 3) and the youngest grains dated in each of the samples overlap in age at 5.596 ± 0.044 Ma (2σ, CCT z10), 5.620 ± 0.021 Ma (Px12-1), and 5.5941 ± 0.0097 Ma (WCT z16; Table 1). Both CCT samples display a narrow range of individual zircon crystallisation ages, while the WCT preserves zircons both younger and older than that range (including one antecryst at 6.028 ± 0.062 Ma). The overlap of all three samples supports their cogenetic identity and allows the derivation of a common maximum estimate of the WCT/CCT eruption age. We consider the crystallisation age of the single youngest zircon (WCT z16) as our best estimate of WCT/CCT eruption age at 5.5941 ± 0.0097 Ma (Fig. 3).

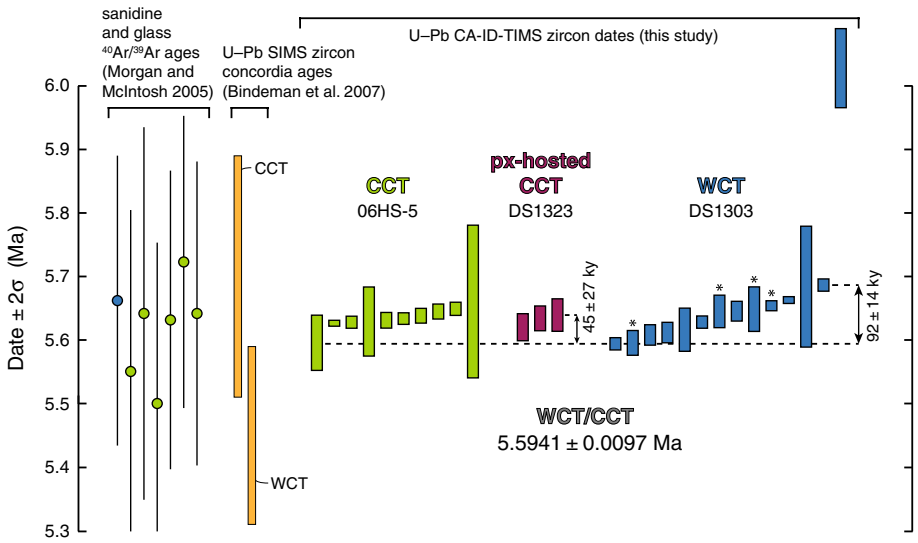

Fig. 3 ID–TIMS U–Pb zircon geochronology of Conant Creek Tuff (CCT) and Wolverine Creek Tuff (WCT). Age-ranked individual zircon $^{206}Pb/^{238}U$ dates are reported with their 2σ analytical uncertainty. The WCT/CCT eruption age estimate of 5.5941 ± 0.0097 Ma (*dashed line*) is based on the date of the youngest WCT/CCT zircon (WCT z16) reported with its 2σ analytical uncertainty, not including tracer and decay constant contributions. *Asterisks* indicate grains of εHf < −10. Shown next to pyroxene-hosted CCT zircon dates is the maximum period of pre-eruptive crystallisation of the pyroxenes; next to WCT dates is a minimum estimate of the duration of pre-eruptive zircon crystallisation. Also shown for comparison are U–Pb zircon concordia ages from Bindeman et al. (2007) and individual $^{40}Ar/^{39}Ar$ eruption ages for both units from Morgan and McIntosh (2005) recalculated using the calibration of Kuiper et al. (2008)

This result is in good agreement with previously published U–Pb SIMS zircon concordia ages of 5.45 ± 0.14 Ma (WCT) and 5.70 ± 0.19 Ma (CCT; Bindeman et al. 2007) and it overlaps within uncertainty with published $^{40}Ar/^{39}Ar$ eruption ages of both units (Morgan and McIntosh 2005) recalculated utilising the calibration of Kuiper et al. (2008) (Fig. 3). Subtracting this ID–TIMS zircon eruption age estimate from the age of the oldest autocrystic zircon (WCT z14) defines the minimum time of pre-eruptive zircon crystallisation as 92 ± 14 ky. Additionally, the recognition that some of the zircons were fully included in CCT clinopyroxene crystals requires that those pyroxenes crystallised not earlier than 45 ± 27 ky before the eruption.

Zircon crystals from both eruptive units are compositionally similar, and both populations exhibit a consistent, age-independent core–rim compositional relationship (Fig. 4). Crystal cores are enriched in all rare earth elements (REE), Y, Ti and depleted in Hf relative to the rims that also display a decrease in Th/U and a more pronounced negative Eu anomaly. The steepness of the heavy element-enriched zircon REE pattern (as depicted by e.g. Yb/Dy ratio for heavy REEs, Fig. 4b) increases from core to rim, which requires a successive depletion of the melt in light and middle REEs relative to HREE. The decrease in Eu/Eu* can be related to the fractionation of feldspar, while the decrease in Th/U and the REE signatures requires the fractionation of apatite or rare thorium- and light REE-enriched accessory phases such as allanite and/or chevkinite.

Ti-in-zircon temperatures obtained using the formulation of Ferry and Watson (2007) show a down-temperature evolution from cores to rims over ~100 °C, between ~800 °C (zircon saturation temperature; Watts et al. 2011) and ~700 °C, with a wide range of temperature in the cores and a limited, lower temperature range in the rims (Fig. 4c). As model inputs, $a_{SiO_2} = 1$ was assumed based on the presence of quartz, while the melt $a_{TiO_2} = 0.5$ was derived using the TiO_2 solubility model of Hayden and Watson (2007) using a major element compositional parameter FM = 1.54 (based on glass compositions), average WCT/CCT glass Ti content (769 ppm; Szymanowski et al. 2015) and a zircon saturation temperature of 800 °C (Watson and Harrison 1983; Watts et al. 2011). Varying a_{TiO_2} by 0.1 results in changing the computed temperatures by ≤25 °C.

In situ oxygen isotope ratios measured in CCT zircons range between $\delta^{18}O = 3.20$ and 4.93‰ with the majority of data clustering at $\delta^{18}O = 3.9$–4.5‰ (Fig. 5a). The O isotopic composition does not vary systematically between crystal cores and rims, nor does it correlate strongly with trace element contents. The in situ data are consistent with previous laser fluorination determinations on bulk CCT zircon separates ($\delta^{18}O = 3.89$, 4.03‰), WCT/CCT sanidine crystals ($\delta^{18}O = 5.19$–6.06‰), and WCT glass ($\delta^{18}O = 6.35$–6.36‰, all Watts et al. 2011), indicating that all mineral phases are close to high-temperature (e.g. 750 °C) oxygen isotopic equilibrium with a normal-$\delta^{18}O$ to

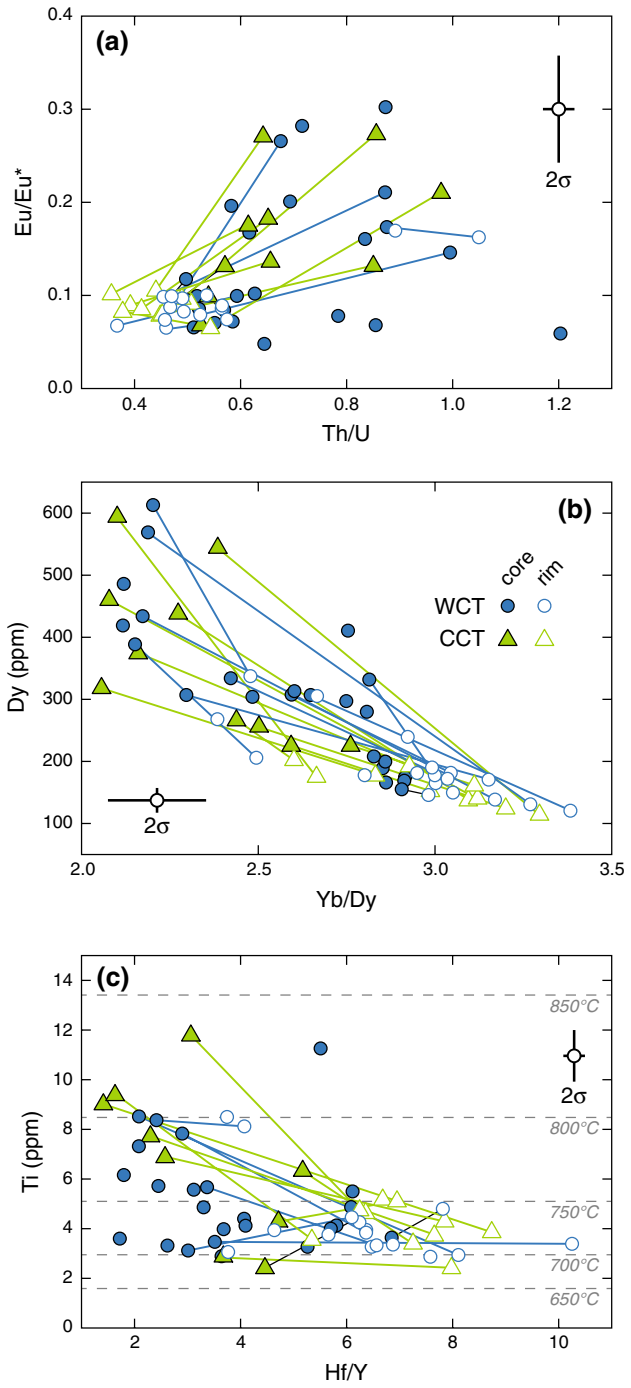

Fig. 4 Trace element (Th/U, Eu/Eu*, Dy, Yb/Dy, Ti, and Hf/Y) variability in WCT/CCT zircons. Where available, analyses of paired cores and rims are joined with lines. Eu/Eu* is controlled by the fractionation of feldspar while Th/U, Yb/Dy, Hf/Y are sensitive to fractionating accessory phases, e.g. apatite, allanite, or chevkinite. Ti is used as a proxy for zircon crystallisation temperature following Ferry and Watson (2007). Typical analytical uncertainties are based on the reproducibility of natural zircon standards. All trace element data are given in the Supplementary material

slightly (~1‰) depleted rhyolitic melt ($\delta^{18}O = 5.7–6.3‰$; Loewen and Bindeman 2016).

Hf isotope ratios in zircon from both CCT samples are homogeneous, while the WCT zircons cluster into at least two distinct populations in εHf–Th/U space (Fig. 5b). Most WCT/CCT zircons belong to a main group at $\varepsilon Hf = -5.0 \pm 2.4$ (2σ), the second WCT population averages $\varepsilon Hf = -12.9 \pm 2.5$ and includes three grains (WCT z6, z11, z21) that appear to be limited in age to ~5.65 Ma as well as a high-Th/U grain (WCT z3) overlapping the eruption age (Table 1; Fig. 3). While no previous Hf isotope values are available for WCT/CCT, the Hf isotopic ratios of most zircons appear consistent with glass εNd values determined by Nash et al. (2006) when related to εHf using the 'terrestrial array' approximation (Vervoort et al. 1999) returning $\varepsilon Hf = -4.1$ for WCT and -4.9 for CCT. The Hf isotopic ratios correlate neither with zircon trace element compositions nor age and are in broad agreement with εHf values of most Yellowstone and Heise zircons measured previously (Wotzlaw et al. 2014, 2015). The presence of multiple zircon populations with distinct Hf isotope compositions in single eruptive units has been noted before in the Huckleberry Ridge Tuff (Wotzlaw et al. 2015; Fig. 5b) and may represent a common feature of Yellowstone–Snake River Plain magmas.

Sr isotopic systematics

Single high-Mg# clinopyroxenes sampled from the Wolverine Creek Tuff, representing the previously described intermediate population remaining in major and trace elemental disequilibrium with the surrounding rhyolitic glass and mineral assemblage (Szymanowski et al. 2015), are also in Sr isotopic disequilibrium with WCT glass measured here and whole rock reported previously (Watts et al. 2011) (Fig. 6; Table 2). Two WCT glass aliquots analysed have $^{87}Sr/^{86}Sr_i = 0.708893$ and 0.708896, which is lower than whole-rock CCT (0.70894) and WCT (0.70947; Watts et al. 2011), both representing some of the least radiogenic YSRP rhyolites so far reported (Fig. 6). The glass has also lower $^{87}Sr/^{86}Sr_i$ than the coexisting WCT/CCT plagioclase previously shown to be in elemental equilibrium (Szymanowski et al. 2015). We note, however, that the LA–MC–ICPMS method used to obtain the plagioclase $^{87}Sr/^{86}Sr$ ratios may overestimate the ratio in comparison with our preferred TIMS data.

The Sr isotopic ratios obtained from nine single high-Mg# WCT pyroxene grains and three multi-grain aliquots of CCT pyroxene range from 0.707047 to 0.708827 (grey band in Fig. 6). The mixed CCT pyroxene samples (Px11,

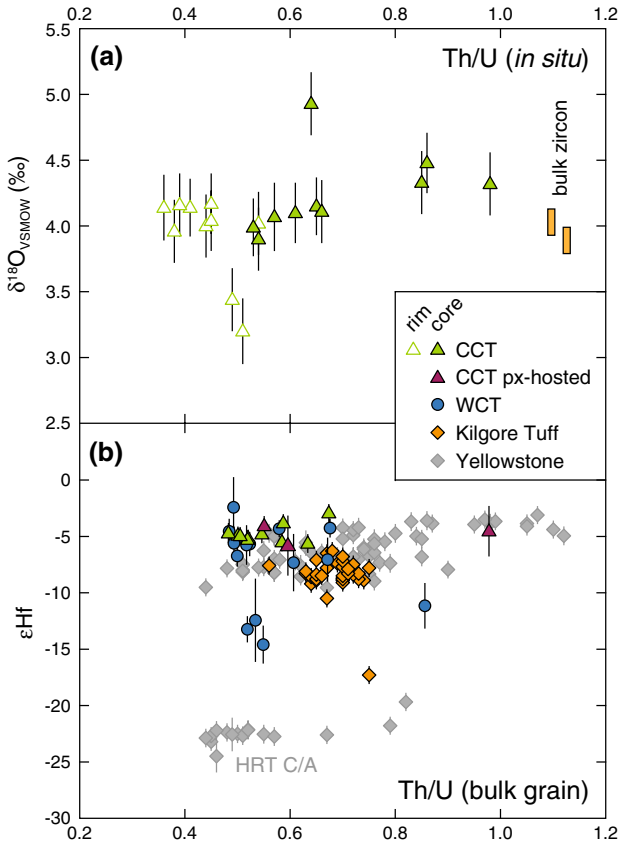

Fig. 5 Trace elemental and isotopic compositions of WCT/CCT zircons. **a** In situ $\delta^{18}O$ and Th/U of CCT zircon cores and rims compared to $\delta^{18}O$ of zircon separates of Watts et al. (2011). **b** Bulk crystal εHf and Th/U of WCT and CCT zircons. Kilgore Tuff data are from Wotzlaw et al. (2014); Yellowstone zircon data including Snake River Butte, Huckleberry Ridge Tuff (HRT), Mesa Falls Tuff, and Lava Creek Tuff eruptions from Wotzlaw et al. (2015). All O and Hf isotopic data are provided in the Supplementary material

Px12, Px19) include both high-Mg# (50–260 ppm Sr) and low-Mg# rhyolitic pyroxenes (3–5 ppm Sr) at variable proportions (in Px19, mass balance requires 4–24% of high-Mg# pyroxenes); therefore, their $^{87}Sr/^{86}Sr_i$ can be considered a mixture of two different signals strongly biased towards the high-Sr, high-Mg# intermediate pyroxene compositions. All $^{87}Sr/^{86}Sr_i$ values measured in WCT/CCT mineral separates are significantly less radiogenic than the host glass, indicating a variable Sr isotopic disequilibrium between these pyroxene crystals and their surrounding melt at the time of eruption. Indeed, the WCT/CCT pyroxene measured here is less radiogenic than any YSRP rhyolites so far reported and has $^{87}Sr/^{86}Sr_i$ values similar to the most radiogenic YSRP basalts found (Fig. 6b).

As a comparison, four multi-grain separates of low-Mg# clinopyroxene from other Heise rhyolites were analysed: the 6.6 Ma Blacktail Creek Tuff (BCT, 3 samples), the 6.2 Ma Lidy Hot Springs lava (LHS, 1), and the 4.5 Ma Kilgore Tuff (KT, 1). Pyroxene from these units is universally near-homogeneous in major and trace elements, with compositions in equilibrium with the rhyolitic melt. The $^{87}Sr/^{86}Sr_i$ values obtained (Table 2) are within the range of YSRP rhyolites (Fig. 6) and in good agreement with the whole-rock ratios of Watts et al. (2011). The only exception to this is the Blacktail Creek Tuff, where the mixed pyroxene separates bracket the bulk $^{87}Sr/^{86}Sr_i$ value of 0.71238 with a spread of 0.71148–0.71299, indicating a possible isotopic disequilibrium within the pyroxene crystal cargo. Overall, the agreement between the isotopic ratios of pyroxene and whole rock from these rhyolites confirms previous results indicating a dominantly equilibrated nature of crystals residing in 'typical' YSRP magmas (Wolff et al. 2011) and reinforcing the unusual nature of the WCT pyroxenes.

Discussion

Common Wolverine Creek–Conant Creek magma reservoir

Despite the differences in the field appearance of the two studied ignimbrites, the strong similarities observed in zircon and pyroxene data presented here indicate provenance of the CCT and the WCT from the same magma reservoir. The correspondence in individual zircon ages (Fig. 3), trace elements (Fig. 4), and Hf isotopic compositions of most zircon crystals (Fig. 5) from both eruptive units requires that all the autocrystic zircons crystallised from a similar (and similarly evolving) rhyolitic melt. While the zircon data set does record inter-crystal Hf isotopic heterogeneities, the age equivalence of the isotopically distinct populations supports the conclusion of a common petrogenesis. The new data support previous interpretations of the equivalence of the WCT and CCT magma reservoirs using glass, feldspar, and pyroxene compositions (Szymanowski et al. 2015), further reinforced by bulk isotope data (Watts et al. 2011) and the overlapping $^{40}Ar/^{39}Ar$ eruption ages (Morgan and McIntosh 2005).

An important petrologic difference between the two units remains in the variable proportions of rhyolitic (low-Mg#) and intermediate, cumulate-derived, high-Mg# pyroxene crystals (Fig. 2), with the WCT being dominated by the intermediate component and the CCT hosting mostly low-Mg# pyroxene (Szymanowski et al. 2015). Reconciling such variations with the uniform melt composition in the WCT and the CCT requires that a recharge bringing the intermediate crystal cargo into the rhyolitic melt is not fully mixed into it, but rather erupted first as the cumulate material-dominated, precursor WCT, followed by the (more voluminous?) rhyolitic material-dominated CCT. We

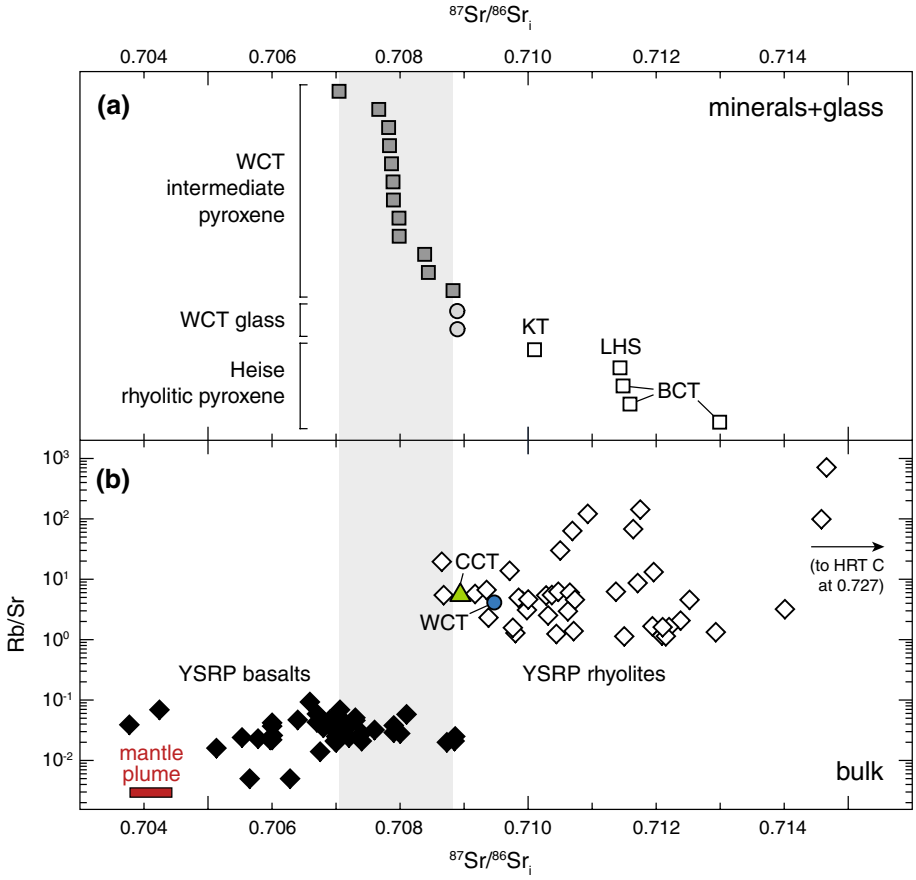

Fig. 6 Strontium isotopic results for pyroxene and glass compared with whole-rock isotopic ratios of YSRP basalts and rhyolites. **a** Ranked $^{87}Sr/^{86}Sr_i$ for pyroxene and glass analysed by TIMS (data presented in Table 2). *KT* Kilgore Tuff, *LHS* Lidy Hot Springs rhyolite, *BCT* Blacktail Creek Tuff. **b** Compilation of whole-rock isotopic data for YSRP basalts and rhyolites; SRP olivine tholeiite data are from Leeman and Manton (1971), Yellowstone basalts and rhyolites from Hildreth et al. (1991), Heise rhyolites from Watts et al. (2011), central SRP rhyolites from Bonnichsen et al. (2008). Note that a few very radiogenic outliers in the rhyolite field reach higher ratios outside of the plot and up to 0.72685 (Huckleberry Ridge Tuff C; Hildreth et al. 1991). Uncertainties are smaller than symbol sizes. The 'mantle plume' represents the most primitive 'Imnaha component' approximating the composition of the Yellowstone mantle plume (Wolff et al. 2008)

propose the WCT may be viewed as an early first phase of a dual WCT/CCT eruption where the welding differences are mainly due to variable fragmentation, transport, and deposition conditions.

Timescales of shallow-crustal magma accumulation

High-precision U–Pb geochronology of single zircons from the WCT/CCT system reveals a history of protracted zircon crystallisation prior to eruption (Fig. 3). We consider the youngest $^{206}Pb/^{238}U$ date of 5.5941 ± 0.0097 Ma as the best estimate for the eruption age of both units. The apparent range of individual zircon crystallisation ages within the larger WCT data set spans 92 ± 14 ky, while the bulk-rock-separated CCT zircons record an apparent spread of 23 ± 11 ky when excluding two relatively imprecise data points at both ends of the age spectrum (CCTz10, z8; Fig. 3). However, taking all the analysed crystals as representative of the same magmatic system, we can consider the larger range of 92 ± 14 ky as our best (minimum) estimate of overall time the rhyolitic melt spent continuously or intermittently zircon-saturated. During this time, the magma crystallised pyroxene, feldspar, and accessory apatite, allanite, and/or chevkinite as indicated by the consistent core–rim trace element zoning profiles in zircon (Fig. 4). The dating of pyroxene-hosted zircons provides an additional clue about the timescales of pyroxene crystallisation in the system; the zircon dates require that many low-Mg# pyroxenes crystallised not earlier than 45 ± 27 ky prior to eruption. This result shows that in Snake River-type systems, zircon may co-crystallise with or predate major phases such as pyroxene, consistent with near-liquidus zircon saturation.

The minimum estimate of 92 ± 14 ky pre-eruptive magma accumulation lends itself to comparison with results from similar systems, such as the Kilgore Tuff erupted from the same Heise eruptive centre (10^3–10^4 years; Wotzlaw et al. 2014) and the super-eruptions of Yellowstone (10^3–10^4 years; Rivera et al. 2014; Wotzlaw et al. 2015). In these cases, the authors interpreted the apparent spreads in individual zircon ages as representing a rapid magma assembly and short storage of upper crustal silicic reservoirs. While such interpretation is plausible also for the WCT/CCT, we note that the 92 ± 14 ky estimate is necessarily a minimum; with zircon a near-liquidus phase, the system may have undergone multiple heating events cyclically pushing it into zircon undersaturation (Cooper and Kent 2014), thus repeatedly crystallising and dissolving zircon crystals (e.g. Bindeman and Melnik 2016).

Table 2 Strontium isotopic compositions of pyroxene and glass analysed by TIMS

Sample	Unit	No. grains/mass	Rb (ppm)	Sr (ppm)	$^{87}Rb/^{86}Sr$	$^{87}Sr/^{86}Sr$	$\pm 2\sigma$	Age (Ma)	$^{87}Sr/^{86}Sr_i$
Rhyolitic glass									
WCT-GL3	Wolverine Creek Tuff	7.1 mg	159.2	15.6	27.92	0.711113	0.000042	5.6	0.708893
WCT-GL4	Wolverine Creek Tuff	9.4 mg	131.8	12.7	30.09	0.711289	0.000062	5.6	0.708896
Rhyolitic (low-Mg#) pyroxene									
BCT-1	Blacktail Creek Tuff	multiple	*<1*	*9 ± 1*	*0.50*	0.711638	0.000074	6.6	0.711591
BCT-2	Blacktail Creek Tuff	multiple	2.0	10.8	0.52	0.713041	0.000035	6.6	0.712992
BCT-3	Blacktail Creek Tuff	multiple	1.7	10.8	0.46	0.711526	0.000028	6.6	0.711483
LHS	Lidy Hot Springs rhyolite	multiple	*<1*	*8 ± 2*	*0.50*	0.711479	0.000016	6.2	0.711435
KT	Kilgore Tuff	multiple	*<1*	*8 ± 1*	*0.50*	0.710132	0.000009	4.5	0.710100
WCT/CCT pyroxene									
Px7	Wolverine Creek Tuff	single	*<1*	*106 ± 36*	*0.10*	0.707055	0.000039	5.6	0.707047
Px9	Wolverine Creek Tuff	single	*<1*	*106 ± 36*	*0.10*	0.708392	0.000033	5.6	0.708384
Px10	Wolverine Creek Tuff	single	*<1*	*106 ± 36*	*0.10*	0.707874	0.000031	5.6	0.707866
Px13	Wolverine Creek Tuff	single	3.0	71.8	0.12	0.708837	0.000021	5.6	0.708827
Px14	Wolverine Creek Tuff	single	7.5	215.6	0.10	0.707994	0.000021	5.6	0.707986
Px15	Wolverine Creek Tuff	single	6.3	236.1	0.08	0.707902	0.000013	5.6	0.707896
Px16	Wolverine Creek Tuff	single	6.8	173.1	0.11	0.708451	0.000049	5.6	0.708442
Px17	Wolverine Creek Tuff	single	3.6	87.4	0.13	0.707677	0.000006	5.6	0.707667
Px18	Wolverine Creek Tuff	single	3.8	100.2	0.11	0.707830	0.000008	5.6	0.707821
Px11	Conant Creek Tuff	multiple	–	–	*0.70*	0.707891	0.000034	5.6	0.707835
Px12	Conant Creek Tuff	multiple	–	–	*0.70*	0.708039	0.000038	5.6	0.707983
Px19	Conant Creek Tuff	multiple	3.5	14.4	0.71	0.707947	0.000010	5.6	0.707890

For WCT samples with high-Sr contents of pyroxene, single grains were analysed; rhyolitic (low-Mg#) pyroxene as well as mixed low-/high-Mg# pyroxene samples of CCT (Px11, Px12, Px19) were larger aliquots of 10–20 grains amounting to a mass of 2–4 mg. Rb and Sr were measured by ID–TIMS for spiked samples; where not available, average concentrations from LA–ICPMS analyses of pyroxene from the same population are given in italics. No estimate is given for Px11 and Px12 as these samples are mixtures of low- and high-Mg# pyroxene. For the purpose of age correction, the $^{87}Rb/^{86}Sr$ of some samples is also assumed based on similarity to other samples and given in italics. Initial $^{87}Sr/^{86}Sr$ ratios ($^{87}Sr/^{86}Sr_i$) are calculated using the measured or assumed $^{87}Rb/^{86}Sr$ and eruption ages of Morgan and McIntosh (2005) with the decay constant $\lambda(^{87}Rb) = 1.42 \times 10^{-11}$ year^{-1} (Steiger and Jäger 1977)

The range in zircon ages could record either (1) the entire lifetime of the erupted magma chamber, or (2) only the last cooling event in an extended life of a heterogeneous upper crustal magma reservoir. Long storage (>10^5 years) of large volumes of magma has been demonstrated for continental arc-related silicic eruptions where magma reservoirs are thought to be stored as near-solidus crystal-rich mush bodies (Vazquez and Reid 2004; Bachmann et al. 2007; Wotzlaw et al. 2013). We speculate that YSRP rhyolitic magmas, while being in many respects different from such arc-related systems (e.g. mineralogy, crystal content of erupted material, volatile contents), may be characterised by broadly comparable storage/crystallisation times. In the case of YSRP, such extended residence in the upper crust may be facilitated by the formation of refractory and mechanically strong mush zones (in places with cumulate characteristics) around the crystal-poor, eruptible melt pockets, partly insulating them from the cold pre-existing wall rocks (Ellis et al. 2014).

Isotopic heterogeneities and the upper crustal architecture of the magma reservoir

Zircons from the WCT/CCT cluster into at least two populations of contrasting Hf isotopic compositions, while overlapping in age within the resolution of our high-precision geochronology. Such relations require the existence of two or more isotopically distinct rhyolite reservoirs that co-existed at the time of eruption and derived their isotopic compositions from variable amounts of assimilation of radiogenic Archean crust during crustal differentiation. A simple two-component mixture model assuming an asthenospheric mantle plume source (Wotzlaw et al. 2015) requires ca. 20 and >30% assimilation of radiogenic Archean crust for the two groups of WCT/CCT zircons with εHf ~ −5 and −13, respectively. The consistency in trace element compositions between the zircon populations of variable εHf suggests similar melt evolution paths with consistent fractionating mineral assemblages, and points

towards similar shallow storage conditions of multiple physically separated batches of melt that either became connected before the eruption or were mixed only during the eruption. Such small-scale sub-chambers can be imagined as multiple comparably sized melt batches or a single dominant melt region with a range of small storage volumes adjacent to chamber roof or walls that would also display variable responses to recharge, crystallisation and wall-rock assimilation. Similar complex multi-batch magmatic architectures of variable proportions have been extensively documented in the Yellowstone–Snake River Plain province based on multiple distinct co-erupted glass or mineral compositional groups (Cathey and Nash 2004; Ellis and Wolff 2012; Ellis et al. 2014; Wotzlaw et al. 2014, 2015) and may represent a common feature of many large-volume volcanic systems worldwide (e.g. Reubi and Nicholls 2005; Shane et al. 2008; Cooper et al. 2012; Bégué et al. 2014).

Isotopic record of crustal assimilation

Evaluating the extent of crustal assimilation in the WCT/CCT recorded by both pyroxenes and zircons requires knowledge of the isotopic characteristics of both the crust and the initial mantle source regions. The bulk of the crust underlying much of the Snake River Plain belongs to old Precambrian basement domains, with the eastern SRP crossing into the Archean Wyoming craton (Foster et al. 2006; McCurry and Rodgers 2009). Sampling of xenoliths within YSRP mafic lavas reveals a spectrum of granulite facies metamorphic lithologies yielding zircon dates between 2.5 and >3.5 Ga (Wolf et al. 2005), variably radiogenic $^{87}Sr/^{86}Sr$ ratios between 0.703 and 0.893, εNd of −52 to −23 (Leeman et al. 1985; McCurry and Rodgers 2009), and 'normal' oxygen isotope signatures of $\delta^{18}O = 6–9‰$ (Watts et al. 2010). In contrast, most of the uppermost crust is thought to be made up of young volcanic rocks produced by the Yellowstone hotspot itself, providing limited leverage in radiogenic isotope ratios (Fig. 6) but exposed to hydrothermal circulation and as such having the potential of delivering large amounts of ^{18}O-depleted material that can be assimilated by new magmas (e.g. Friedman et al. 1974; Hildreth et al. 1984; Bindeman and Valley 2001; Watts et al. 2011; Boroughs et al. 2012). The isotopic composition of the mantle-derived melts can be approximated by the compositions of YSRP olivine tholeiites (Fig. 6); however, their relatively radiogenic nature ($^{87}Sr/^{86}Sr = 0.704–0.709$) suggests that much of the radiogenic isotope signal in the YSRP melts may be derived already from deep plume–lithosphere interaction (Doe et al. 1982; Hanan et al. 2008; Jean et al. 2014).

As presented above, the WCT/CCT has one of the lowest bulk and glass $^{87}Sr/^{86}Sr$ and εNd among YSRP rhyolites (one of the most primitive YSRP rhyolites; Fig. 6). It also displays a normal to moderately light O isotope composition (Watts et al. 2011). Both these facts suggest relatively minor assimilation of both Archean source materials and previously erupted (and possibly hydrothermally altered) volcanic materials (cf. Watts et al. 2011), assuming an initial melt similar to the relatively radiogenic YSRP basalts. The WCT/CCT magma therefore seems to have evolved dominantly through polybaric fractional crystallisation, with the limited isotopic shift more likely achieved by assimilating small amounts of fertile Archean crust rather than young, shallow volcanic rocks. Localised portions of melt at εHf < −10 (as recorded by WCT/CCT zircons) additionally support a prevailing role of Archean source material as assimilant.

A chemical evolution dominantly controlled by fractional crystallisation is further supported by the unique record of 'intermediate' WCT pyroxenes, which span a range of compositions between Mg# 60–90 corresponding to equilibrium crystallisation from mafic to intermediate melts (Szymanowski et al. 2015) while covering a range of $^{87}Sr/^{86}Sr$ ratios typical for the most radiogenic YSRP basalts to the least radiogenic YSRP rhyolites. The single-grain Sr isotopic record thus indicates dominantly lower- to mid-crustal assimilation consistent with previous petrological conclusions about intermediate storage and differentiation levels (Szymanowski et al. 2015) as well as a growing amount of geophysical evidence for high-crystallinity, low-melt fraction magmatic bodies occurring throughout the crustal column in association with eruptive centres of the Yellowstone–Snake River Plain volcanic province (Sparlin et al. 1982; Peng and Humphreys 1998; DeNosaquo et al. 2009; Farrell et al. 2014; Huang et al. 2015).

Conclusions

Our combined study of zircon and pyroxene crystals in the Wolverine Creek–Conant Creek system reveals a complex record of magma–crust interaction in a crustal-scale magmatic system and helps to paint a picture of the evolution of Yellowstone–Snake River Plain magmas when unaffected by the shallow-crustal influence of hydrothermally altered materials. The compositions of the high-Mg# pyroxene and melt inclusions support the predominance of fractional crystallisation processes in producing the rhyolites, which is consistent with geophysical imaging of high-crystallinity intermediate storage levels underlying the YSRP eruptive centres throughout the whole crust. The new data set of Sr isotopes in WCT/CCT pyroxene presented here shows that (1) the amount of assimilation of Archean crust into the YSRP melts is limited, and (2) it may occur dominantly in the lower- and mid-crust while the melt evolves from primitive basalts towards more silicic compositions.

Variably radiogenic Hf isotope ratios in zircon between $\varepsilon Hf = -2$ and -15 indicate that the WCT/CCT was derived by amalgamation of at least two isotopically distinct melt domains derived by assimilating slightly different amounts of Archean crust. Such melts evolved towards rhyolitic compositions finally stored at a shallow-crustal level where they retained zircons for a minimum of 92 ± 14 ky. The final WCT/CCT eruption sampled an upper crustal magma reservoir in which isotopically distinct but compositionally similar rhyolitic liquids were stored separately prior to mixing upon eruption. Such multi-batch architectures of magmatic reservoirs appear to be a common feature of high-temperature rhyolites of the Yellowstone–Snake River Plain area and possibly other volcanic systems in similar tectonic settings.

Acknowledgements This work has been supported by Swiss National Science Foundation Grant 200021_155923. J. F. W. acknowledges funding through the ETH Zürich Postdoctoral Fellowship program. We would like to thank M. Guillong for help with LA–ICPMS analyses, F. X. d'Abzac (UNIGE), S. Large, and H. F. Robert (ETH) for help during Hf isotope measurements, and R. A. Stern for oxygen isotope analyses. We appreciate constructive reviews by C. Bucholz and F. Corfu as well as the editorial handling of O. Müntener.

References

Anders MH, Rodgers DW, Hemming SR, Saltzman J, DiVenere VJ, Hagstrum JT, Embree GF, Walter RC (2014) A fixed sublithospheric source for the late Neogene track of the Yellowstone hotspot: implications of the Heise and Picabo volcanic fields. J Geophys Res 119:2871–2906. doi:10.1002/2013jb010483

Bachmann O, Bergantz GW (2004) On the origin of crystal-poor rhyolites: extracted from batholithic crystal mushes. J Petrol 45:1565–1582. doi:10.1093/petrology/egh019

Bachmann O, Bergantz GW (2008) Rhyolites and their source mushes across tectonic settings. J Petrol 49:2277–2285. doi:10.1093/petrology/egn068

Bachmann O, Oberli F, Dungan M, Meier M, Mundil R, Fischer H (2007) $^{40}Ar/^{39}Ar$ and U–Pb dating of the Fish Canyon magmatic system, San Juan Volcanic field, Colorado: evidence for an extended crystallization history. Chem Geol 236:134–166. doi:10.1016/j.chemgeo.2006.09.005

Bégué F, Deering CD, Gravley DM, Kennedy BM, Chambefort I, Gualda GAR, Bachmann O (2014) Extraction, storage and eruption of multiple isolated magma batches in the paired Mamaku and Ohakuri eruption, Taupo Volcanic Zone, New Zealand. J Petrol 55(8):1653–1684. doi:10.1093/petrology/egu038

Bindeman IN, Melnik OE (2016) Zircon survival, rebirth and recycling during crustal melting, magma crystallization, and mixing based on numerical modelling. J Petrol 57(3):437–459. doi:10.1093/petrology/egw013

Bindeman IN, Valley JW (2001) Low-$\delta^{18}O$ rhyolites from Yellowstone: magmatic evolution based on analyses of zircons and individual phenocrysts. J Petrol 42:1491–1517. doi:10.1093/petrology/42.8.1491

Bindeman IN, Watts KE, Schmitt AK, Morgan LA, Shanks PWC (2007) Voluminous low $\delta^{18}O$ magmas in the late Miocene Heise volcanic field, Idaho: implications for the fate of Yellowstone hotspot calderas. Geology 35:1019–1022. doi:10.1130/g24141a.1

Black LP, Kamo SL, Allen CM, Davis DW, Aleinikoff JN, Valley JW, Mundil R, Campbell IH, Korsch RJ, Williams IS (2004) Improved $^{206}Pb/^{238}U$ microprobe geochronology by the monitoring of a trace-element-related matrix effect; SHRIMP, ID–TIMS, ELA–ICP–MS and oxygen isotope documentation for a series of zircon standards. Chem Geol 205(1):115–140. doi:10.1016/j.chemgeo.2004.01.003

Bohrson WA, Spera FJ, Ghiorso MS, Brown GA, Creamer JB, Mayfield A (2014) Thermodynamic model for energy-constrained open-system evolution of crustal magma bodies undergoing simultaneous recharge, assimilation and crystallization: the Magma Chamber Simulator. J Petrol 55(9):1685–1717. doi:10.1093/petrology/egu036

Bolte T, Holtz F, Almeev R, Nash B (2015) The Blacktail Creek Tuff: an analytical and experimental study of rhyolites from the Heise volcanic field, Yellowstone hotspot system. Contrib Mineral Petrol 169:1–24. doi:10.1007/s00410-015-1112-0

Bonnichsen B, Leeman WP, Honjo N, McIntosh WC, Godchaux MM (2008) Miocene silicic volcanism in southwestern Idaho: geochronology, geochemistry, and evolution of the central Snake River Plain. Bull Volcanol 70:315–342. doi:10.1007/s00445-007-0141-6

Boroughs S, Wolff J, Bonnichsen B, Godchaux M, Larson P (2005) Large-volume, low-$\delta^{18}O$ rhyolites of the central Snake River Plain, Idaho, USA. Geology 33(10):821–824. doi:10.1130/G21723.1

Boroughs S, Wolff JA, Ellis BS, Bonnichsen B, Larson PB (2012) Evaluation of models for the origin of Miocene low-$\delta^{18}O$ rhyolites of the Yellowstone/Columbia River Large Igneous Province. Earth Planet Sci Lett 313–314:45–55. doi:10.1016/j.epsl.2011.10.039

Bowring JF, McLean NM, Bowring SA (2011) Engineering cyber infrastructure for U–Pb geochronology: Tripoli and U–Pb_Redux. Geochem Geophys Geosyst 12:Q0AA19. doi:10.1029/2010GC003479

Branney MJ, Bonnichsen B, Andrews GDM, Ellis B, Barry TL, McCurry M (2008) 'Snake River (SR)-type' volcanism at the Yellowstone hotspot track: distinctive products from unusual, high-temperature silicic super-eruptions. Bull Volcanol 70:293–314. doi:10.1007/s00445-007-0140-7

Brown SJA, Fletcher IR (1999) SHRIMP U–Pb dating of the preeruption growth history of zircons from the 340 ka Whakamaru Ignimbrite, New Zealand: evidence for >250 ky magma residence times. Geology 27(11):1035–1038. doi:10.1130/0091-7613(1999)027<1035:supdot>2.3.co;2

Cathey HE, Nash BP (2004) The Cougar Point Tuff: implications for thermochemical zonation and longevity of high-temperature, large-volume silicic magmas of the Miocene Yellowstone hotspot. J Petrol 45:27–58. doi:10.1093/petrology/egg081

Christiansen RL (2001) The Quaternary and Pliocene Yellowstone Plateau volcanic field of Wyoming, Idaho, and Montana. US Geol Surv Prof Paper 729-G

Christiansen EH, McCurry M (2008) Contrasting origins of Cenozoic silicic volcanic rocks from the western Cordillera of the United States. Bull Volcanol 70:251–267. doi:10.1007/s00445-007-0138-1

Claiborne LL, Miller CF, Flanagan DM, Clynne MA, Wooden JL (2010) Zircon reveals protracted magma storage and recycling beneath Mount St. Helens. Geology 38:1011–1014. doi:10.1130/G31285.1

Condon DJ, Schoene B, McLean NM, Bowring SA, Parrish RR (2015) Metrology and traceability of U–Pb isotope dilution geochronology (EARTHTIME tracer calibration part I). Geochim Cosmochim Acta 164:464–480. doi:10.1016/j.gca.2015.05.026

Cooper KM, Kent AJR (2014) Rapid remobilization of magmatic crystals kept in cold storage. Nature 506(7489):480–483. doi:10.1038/nature12991

Cooper GF, Wilson CJN, Millet MA, Baker JA, Smith EGC (2012) Systematic tapping of independent magma chambers during the 1 Ma Kidnappers supereruption. Earth Planet Sci Lett 313–314:23–33. doi:10.1016/j.epsl.2011.11.006

D'Abzac FX, Davies JHFL, Wotzlaw JF, Schaltegger U (2016) Hf isotope analysis of small zircon and baddeleyite grains by conventional Multi Collector-Inductively Coupled Plasma-Mass Spectrometry. Chem Geol 433:12–23. doi:10.1016/j.chemgeo.2016.03.025

DeNosaquo KR, Smith RB, Lowry AR (2009) Density and lithospheric strength models of the Yellowstone–Snake River Plain volcanic system from gravity and heat flow data. J Volcanol Geoth Res 188:108–127. doi:10.1016/j.jvolgeores.2009.08.006

Doe BR, Leeman WP, Christiansen RL, Hedge CE (1982) Lead and strontium isotopes and related trace elements as genetic tracers in the Upper Cenozoic rhyolite-basalt association of the Yellowstone Plateau Volcanic Field. J Geophys Res 87:4785–4806. doi:10.1029/JB087iB06p04785

Ellis BS, Wolff JA (2012) Complex storage of rhyolite in the central Snake River Plain. J Volcanol Geoth Res 211–212:1–11. doi:10.1016/j.jvolgeores.2011.10.002

Ellis BS, Wolff JA, Boroughs S, Mark DF, Starkel WA, Bonnichsen B (2013) Rhyolitic volcanism of the central Snake River Plain: a review. Bull Volcanol 75:745. doi:10.1007/s00445-013-0745-y

Ellis BS, Bachmann O, Wolff JA (2014) Cumulate fragments in silicic ignimbrites: the case of the Snake River Plain. Geology 42:431–434. doi:10.1130/g35399.1

Farrell J, Smith RB, Husen S, Diehl T (2014) Tomography from 26 years of seismicity revealing that the spatial extent of the Yellowstone crustal magma reservoir extends well beyond the Yellowstone caldera. Geophys Res Lett 41(9):3068–3073. doi:10.1002/2014GL059588

Ferry JM, Watson EB (2007) New thermodynamic models and revised calibrations for the Ti-in-zircon and Zr-in-rutile thermometers. Contrib Mineral Petrol 154(4):429–437. doi:10.1007/s00410-007-0201-0

Foster DA, Mueller PA, Mogk DW, Wooden JL, Vogl JJ (2006) Proterozoic evolution of the western margin of the Wyoming craton: implications for the tectonic and magmatic evolution of the northern Rocky Mountains. Can J Earth Sci 43(10):1601–1619. doi:10.1139/e06-052

Friedman I, Lipman PW, Obradovich JD, Gleason JD, Christiansen RL (1974) Meteoric water in magmas. Science 184(4141):1069–1072. doi:10.1126/science.184.4141.1069

Gelman SE, Gutierrez FJ, Bachmann O (2013) On the longevity of large upper crustal silicic magma reservoirs. Geology 41:759–762. doi:10.1130/g34241.1

Gerstenberger H, Haase G (1997) A highly effective emitter substance for mass spectrometric Pb isotope ratio determinations. Chem Geol 136:309–312. doi:10.1016/S0009-2541(96)00033-2

Guillong M, von Quadt A, Sakata S, Peytcheva I, Bachmann O (2014) LA–ICP–MS Pb–U dating of young zircons from the Kos–Nisyros volcanic centre, SE Aegean arc. J Anal At Spectrom 29:963–970. doi:10.1039/C4JA00009A

Hanan BB, Shervais JW, Vetter SK (2008) Yellowstone plume-continental lithosphere interaction beneath the Snake River Plain. Geology 36(1):51–54. doi:10.1130/G23935a.1

Hayden LA, Watson EB (2007) Rutile saturation in hydrous siliceous melts and its bearing on Ti-thermometry of quartz and zircon. Earth Planet Sci Lett 258(3–4):561–568. doi:10.1016/j.epsl.2007.04.020

Hiess J, Condon DJ, McLean N, Noble SR (2012) $^{238}U/^{235}U$ systematics in terrestrial uranium-bearing minerals. Science 335(6076):1610–1614. doi:10.1126/science.1215507

Hildreth W (2004) Volcanological perspectives on Long Valley, Mammoth Mountain, and Mono Craters: several contiguous but discrete systems. J Volcanol Geoth Res 136(3–4):169–198. doi:10.1016/j.jvolgeores.2004.05.019

Hildreth W, Christiansen RL, O'Neil JR (1984) Catastrophic isotopic modification of rhyolitic magma at times of caldera subsidence, Yellowstone Plateau volcanic field. J Geophys Res 89:8339–8369. doi:10.1029/JB089iB10p08339

Hildreth W, Halliday AN, Christiansen RL (1991) Isotopic and chemical evidence concerning the genesis and contamination of basaltic and rhyolitic magma beneath the Yellowstone Plateau volcanic field. J Petrol 32:63–138. doi:10.1093/petrology/32.1.63

Huang H-H, Lin F-C, Schmandt B, Farrell J, Smith RB, Tsai VC (2015) The Yellowstone magmatic system from the mantle plume to the upper crust. Science 348(6236):773–776. doi:10.1126/science.aaa5648

Jaffey AH, Flynn KF, Glendenin LE, Bentley WC, Essling AM (1971) Precision measurement of half-lives and specific activities of ^{235}U and ^{238}U. Phys Rev C 4(5):1889. doi:10.1103/PhysRevC.4.1889

Jean MM, Hanan BB, Shervais JW (2014) Yellowstone hotspot-continental lithosphere interaction. Earth Planet Sci Lett 389:119–131. doi:10.1016/j.epsl.2013.12.012

Krogh TE (1973) A low-contamination method for hydrothermal decomposition of zircon and extraction of U and Pb for isotopic age determinations. Geochim Cosmochim Acta 37:485–494. doi:10.1016/0016-7037(73)90213-5

Kuiper KF, Deino A, Hilgen FJ, Krijgsman W, Renne PR, Wijbrans JR (2008) Synchronizing rock clocks of Earth history. Science 320(5875):500–504. doi:10.1126/science.1154339

Leeman WP, Manton WI (1971) Strontium isotopic composition of basaltic lavas from the Snake River Plain, southern Idaho. Earth Planet Sci Lett 11:420–434. doi:10.1016/0012-821X(71)90204-4

Leeman WP, Menzies MA, Matty DJ, Embree GF (1985) Strontium, neodymium and lead isotopic compositions of deep crustal xenoliths from the Snake River Plain: evidence for Archean basement. Earth Planet Sci Lett 75:354–368. doi:10.1016/0012-821x(85)90179-7

Loewen MW, Bindeman IN (2016) Oxygen isotope thermometry reveals high magmatic temperatures and short residence times in Yellowstone and other hot-dry rhyolites compared to cold-wet systems. Am Mineral 101(5–6):1222–1227. doi:10.2138/am-2016-5591

Mahood GA (1990) Second reply to comment of R.S.J. Sparks, H.E. Huppert and C.J.N. Wilson on "Evidence for long residence times of rhyolitic magma in the Long Valley magmatic system: the isotopic record in the precaldera lavas of Glass Mountain". Earth Planet Sci Lett 99(4):395–399. doi:10.1016/0012-821X(90)90145-N

Marsh BD (1981) On the crystallinity, probability of occurrence, and rheology of lava and magma. Contrib Mineral Petrol 78(1):85–98. doi:10.1007/bf00371146

Mattinson JM (2005) Zircon U–Pb chemical abrasion ("CA-TIMS") method: combined annealing and multi-step partial dissolution analysis for improved precision and accuracy of zircon ages. Chem Geol 220:47–66. doi:10.1016/j.chemgeo.2005.03.011

McCurry M, Rodgers DW (2009) Mass transfer along the Yellowstone hotspot track I: petrologic constraints on the volume of mantle-derived magma. J Volcanol Geoth Res 188:86–98. doi:10.1016/j.jvolgeores.2009.04.001

McLean NM, Bowring JF, Bowring SA (2011) An algorithm for U-Pb isotope dilution data reduction and uncertainty propagation. Geochem Geophys Geosyst 12:Q0AA18. doi:10.1029/2010GC003478

McLean NM, Condon DJ, Schoene B, Bowring SA (2015) Evaluating uncertainties in the calibration of isotopic reference materials

and multi-element isotopic tracers (EARTHTIME tracer calibration part II). Geochim Cosmochim Acta 164:481–501. doi:10.1016/j.gca.2015.02.040

Morgan LA, McIntosh WC (2005) Timing and development of the Heise volcanic field, Snake River Plain, Idaho, western USA. Geol Soc Am Bull 117:288–306. doi:10.1130/b25519.1

Nash BP, Perkins ME, Christensen JN, Lee D-C, Halliday AN (2006) The Yellowstone hotspot in space and time: Nd and Hf isotopes in silicic magmas. Earth Planet Sci Lett 247:143–156. doi:10.1016/j.epsl.2006.04.030

Peng X, Humphreys ED (1998) Crustal velocity structure across the eastern Snake River Plain and the Yellowstone swell. J Geophys Res 103:7171–7186. doi:10.1029/97jb03615

Phillips WM, Moore DK, Feeney DM, Embree GF (2016) Geologic map of the Heise quadrangle, Bonneville, Jefferson, and Madison counties, Idaho. Idaho Geol Surv Digital Web Map 176, scale 1:24,000

Pin C, Briot D, Bassin C, Poitrasson F (1994) Concomitant separation of strontium and samarium-neodymium for isotopic analysis in silicate samples, based on specific extraction chromatography. Anal Chim Acta 298:209–217. doi:10.1016/0003-2670(94)00274-6

Reid MR, Coath CD, Harrison TM, McKeegan KD (1997) Prolonged residence times for the youngest rhyolites associated with Long Valley Caldera: ^{230}Th–^{238}U ion microprobe dating of young zircons. Earth Planet Sci Lett 150:27–39. doi:10.1016/S0012-821X(97)00077-0

Reubi O, Nicholls IA (2005) Structure and dynamics of a silicic magmatic system associated with caldera-forming eruptions at Batur volcanic field, Bali, Indonesia. J Petrol 46(7):1367–1391. doi:10.1093/petrology/egi019

Rivera TA, Schmitz MD, Crowley JL, Storey M (2014) Rapid magma evolution constrained by zircon petrochronology and ^{40}Ar/^{39}Ar sanidine ages for the Huckleberry Ridge Tuff, Yellowstone, USA. Geology 42:643–646. doi:10.1130/G35808.1

Scherer E, Münker C, Mezger K (2001) Calibration of the lutetium–hafnium clock. Science 293(5530):683–687. doi:10.1126/science.1061372

Shane P, Nairn IA, Smith VC, Darragh M, Beggs K, Cole JW (2008) Silicic recharge of multiple rhyolite magmas by basaltic intrusion during the 22.6 ka Okareka Eruption Episode, New Zealand. Lithos 103(3):527–549. doi:10.1016/j.lithos.2007.11.002

Simakin AG, Bindeman IN (2012) Remelting in caldera and rift environments and the genesis of hot, "recycled" rhyolites. Earth Planet Sci Lett 337–338:224–235. doi:10.1016/j.epsl.2012.04.011

Sparlin MA, Braile LW, Smith RB (1982) Crustal structure of the eastern Snake River Plain determined from ray trace modeling of seismic refraction data. J Geophys Res 87:2619–2633. doi:10.1029/JB087iB04p02619

Stefano CJ, Mukasa SB, Andronikov A, Leeman WP (2010) Water and other volatile systematics of olivine-hosted melt inclusions from the Yellowstone hotspot track. Contrib Mineral Petrol 161:615–633. doi:10.1007/s00410-010-0553-8

Steiger RH, Jäger E (1977) Subcommission on geochronology: convention on the use of decay constants in geo- and cosmochronology. Earth Planet Sci Lett 36:359–362. doi:10.1016/0012-821X(77)90060-7

Szymanowski D, Ellis BS, Bachmann O, Guillong M, Phillips WM (2015) Bridging basalts and rhyolites in the Yellowstone–Snake River Plain volcanic province: the elusive intermediate step. Earth Planet Sci Lett 415:80–89. doi:10.1016/j.epsl.2015.01.041

Thompson AB, Matile L, Ulmer P (2002) Some thermal constraints on crustal assimilation during fractionation of hydrous, mantle-derived magmas with examples from central Alpine batholiths. J Petrol 43(3):403–422. doi:10.1093/petrology/43.3.403

Vazquez JA, Reid MR (2004) Probing the accumulation history of the voluminous Toba magma. Science 305(5686):991–994. doi:10.1126/science.1096994

Vervoort JD, Blichert-Toft J (1999) Evolution of the depleted mantle: Hf isotope evidence from juvenile rocks through time. Geochim Cosmochim Acta 63(3):533–556. doi:10.1016/S0016-7037(98)00274-9

Vervoort JD, Patchett PJ, Blichert-Toft J, Albarède F (1999) Relationships between Lu–Hf and Sm–Nd isotopic systems in the global sedimentary system. Earth Planet Sci Lett 168(1–2):79–99. doi:10.1016/S0012-821X(99)00047-3

von Quadt A, Wotzlaw JF, Buret Y, Large SJE, Peytcheva I, Trinquier A (2016) High-precision zircon U/Pb geochronology by ID–TIMS using new 10^{13} ohm resistors. J Anal At Spectrom 31(3):658–665. doi:10.1039/c5ja00457h

Watson EB, Harrison TM (1983) Zircon saturation revisited: temperature and composition effects in a variety of crustal magma types. Earth Planet Sci Lett 64(2):295–304. doi:10.1016/0012-821x(83)90211-X

Watts KE, Leeman WP, Bindeman IN, Larson PB (2010) Supereruptions of the Snake River Plain: two-stage derivation of low-δ^{18}O rhyolites from normal-δ^{18}O crust as constrained by Archean xenoliths. Geology 38:503–506. doi:10.1130/g30735.1

Watts KE, Bindeman IN, Schmitt AK (2011) Large-volume rhyolite genesis in caldera complexes of the Snake River Plain: insights from the Kilgore Tuff of the Heise volcanic field, Idaho, with comparison to Yellowstone and Bruneau–Jarbidge rhyolites. J Petrol 52:857–890. doi:10.1093/petrology/egr005

Wolf DE, Leeman WP, Vervoort JD (2005) U–Pb zircon geochronology of crustal xenoliths confirms presence of Archean basement beneath the central and eastern Snake River Plain. Geol Soc Am Abstr Prog 37(7):60

Wolff JA, Ramos FC, Hart GL, Patterson JD, Brandon AD (2008) Columbia River flood basalts from a centralized crustal magmatic system. Nat Geosci 1:177–180. doi:10.1038/ngeo124

Wolff JA, Ellis BS, Ramos FC (2011) Strontium isotopes and magma dynamics: insights from high-temperature rhyolites. Geology 39:931–934. doi:10.1130/g32062.1

Wolff JA, Ellis BS, Ramos FC, Starkel WA, Boroughs S, Olin PH, Bachmann O (2015) Remelting of cumulates as a process for producing chemical zoning in silicic tuffs: a comparison of cool, wet and hot, dry rhyolitic magma systems. Lithos 236–237:275–286. doi:10.1016/j.lithos.2015.09.002

Wotzlaw JF, Schaltegger U, Frick DA, Dungan MA, Gerdes A, Günther D (2013) Tracking the evolution of large-volume silicic magma reservoirs from assembly to supereruption. Geology 41:867–870. doi:10.1130/G34366.1

Wotzlaw JF, Bindeman IN, Watts KE, Schmitt AK, Caricchi L, Schaltegger U (2014) Linking rapid magma reservoir assembly and eruption trigger mechanisms at evolved Yellowstone-type supervolcanoes. Geology 42:807–810. doi:10.1130/G35979.1

Wotzlaw JF, Bindeman IN, Stern RA, D'Abzac FX, Schaltegger U (2015) Rapid heterogeneous assembly of multiple magma reservoirs prior to Yellowstone supereruptions. Sci Rep 5:14026. doi:10.1038/srep14026